Materials Horizons

ROYAL SOCIETY OF CHEMISTRY

COMMUNICATION

View Article Online
View Journal

Cite this: DOI: 10.1039/d5mh01168j

Received 18th June 2025,
Accepted 18th July 2025

DOI: 10.1039/d5mh01168j

rsc.li/materials-horizons

Ferroelectric small molecule enabled high-performance zinc-ion batteries†

Lixin Song,‡[a] Ruizhe Zhang,‡[a] Zhiyong Liao,‡[a] Yongbo Fan,*[b] Yawen Li,[a] Longtao Ma[c] and Huiqing Fan*[a]

To address the challenges of zinc-anode corrosion, hydrogen evolution reactions and dendrite growth in aqueous zinc-ion batteries, we introduce tetraethylammonium perchlorate (TEACC) as ferroelectric small molecules additives in an aqueous electrolyte. The TEACC molecules partially replace water molecules in the Zn^{2+} solvation sheath and enrich the electrode/electrolyte interface with TEACC–OTf, creating a water-deficient inner Helmholtz plane. As a result, the activity of free water is suppressed and the hydrogen-evolution potential shifts from −0.124 V to −0.271 V *versus* Zn/Zn^{2+}. This interfacial restructuring also facilitates the *in situ* formation of a stable solid electrolyte interphase (SEI) consisting of $ZnCO_3$, $ZnCl_2$ and ZnS compounds, promoting highly reversible Zn plating/stripping with the coulombic efficiency exceeding 99.5%. Furthermore, the inherent ferroelectric properties of TEACC generate localized electric fields that help homogenize the distribution of Zn^{2+} across the electrode surface. This effectively suppresses dendritic growth and reduces the Zn^{2+} nucleation overpotential by 35 mV. Electrochemical evaluation of full cells with Zn‖$TBABr_3$ demonstrated impressive performance, with 92.94% capacity retention after 380 cycles at 1.25 A g^{-1} and excellent rate capability across current densities from 0.5 to 3 A g^{-1}. The system's practical applicability was further validated through flexible pouch cell configurations, where two series-connected cells powered 32 commercial LED indicators, showcasing the potential of this approach for flexible energy storage devices. Overall, the findings not only present a promising strategy for stabilizing zinc anode interfaces but also highlight the potential of ferroelectric molecular additives in advanced aqueous battery systems.

New concepts

This research presents a novel approach for stabilizing zinc anodes in aqueous zinc-ion batteries through the incorporation of ferroelectric small molecule additives, specifically tetraethylammonium perchlorate (TEACC), into an electrolyte. The broader impacts of this work extend across environmental sustainability, technological advancement, and societal benefits. Environmentally, the use of water-based electrolytes and non-toxic ferroelectric additives contributes to the development of safer, more sustainable alternatives to flammable organic systems, aligning with global efforts to decarbonize energy storage. Technologically, the introduction of TEACC enables significant improvements in interfacial stability, dendrite suppression, and coulombic efficiency (>99.5%), offering a robust path toward long-lifetime and high-rate zinc-based batteries. These improvements are directly relevant for applications such as grid-scale energy storage, wearable electronics, and emergency power systems. The successful demonstration of flexible pouch cells capable of powering commercial LEDs further reinforces the feasibility of this strategy in real-world scenarios. Moreover, the interdisciplinary nature of the work—spanning electrochemistry, materials science, and interface engineering—contributes to the training of highly skilled researchers and promotes knowledge transfer into clean energy innovation pipelines. This research thus represents a critical step forward in the realization of affordable, safe, and high-performance aqueous energy storage technologies for a low-carbon future.

1. Introduction

Under the dual pressures of the global energy crisis and environmental pollution, the development of efficient and environmentally sustainable energy storage systems has emerged as one of the most prominent research areas.[1–3] Among various energy storage technologies, rechargeable batteries have gained prominence due to their stable and efficient

[a] State Key Laboratory of Solidification Processing, School of Materials Science and Engineering, Northwestern Polytechnical University, Xi'an 710072, P. R. China. E-mail: hqfan@nwpu.edu.cn
[b] Department of Applied Physics, The Hong Kong Polytechnic University, Hung Hom, Hong Kong, 100872, P. R. China. E-mail: fanybmail@163.com
[c] School of Materials Science and Engineering, Guangdong Provincial Key Laboratory of Advanced Energy Storage Materials, South China University of Technology, Guangzhou 510641, P. R. China

† Electronic supplementary information (ESI) available. See DOI: https://doi.org/10.1039/d5mh01168j

‡ L. Song, R. Zhang and Z. Liao contributed equally to this work.

energy conversion capabilities.[4,5] Particularly, aqueous zinc-ion batteries (AZIBs) have garnered considerable attention from researchers due to their low redox potential (−0.76 V *vs.* SHE), high safety, low cost, high theoretical specific capacity (820 mAh g^{-1} or 5855 mAh cm^{-3}), and environmentally friendly nature.[6–10] However, the performance of aqueous zinc-ion batteries is limited by the low decomposition voltage of water (~1.23 V), which results in a narrow electrochemical window.[11,12] Additionally, the coulombic efficiency of zinc plating/stripping in aqueous electrolytes is relatively low.[13,14] The zinc anode is susceptible to corrosion, hydrogen evolution, and the accumulation of by-products, leading to non-uniform zinc deposition and an uneven electric field distribution. These factors accelerate dendrite growth, ultimately causing premature battery failure.

To overcome the existing technical challenges in AZIBs, extensive global research efforts have yielded significant advancements, particularly in electrolyte engineering. Several innovative strategies have been developed, including solid-state electrolytes,[15–18] concentrated "water-in-salt" electrolytes,[19–21] gel polymer electrolytes,[22–24] functional additives,[25–27] ionic liquids, and deep eutectic solvents (DESs).[28–30] Among these approaches, the incorporation of functional additives stands out as a particularly promising solution due to its simplicity, cost-effectiveness, and operational efficiency. These additives function by directly modulating the electrochemical reaction environment, enabling dynamic regulation of the electrochemical interface stability, which consequently enhances the adaptability of the battery to diverse operating conditions and improves the overall performance metrics. Ferroelectric materials, with their high dielectric constant and spontaneous polarization, have attracted considerable research interest. Their large dielectric constant can effectively suppress the formation of space charge layers, thereby enhancing the transport efficiency of metal ions. Additionally, ferroelectric molecules adsorbed on the metal anode can generate a localized built-in electric field. During downward polarization, the electric field lines point from the metallic protrusions toward the zinc anode, driving Zn^{2+} ions to migrate to the base of the protrusions. This reduces the "tip effect," thereby suppressing dendrite growth.[31,32] Moreover, given the piezoelectric nature of ferroelectric materials, their volume changes can be strategically utilized to regulate ion transport at the cathode. When deposited on a substrate, piezoelectric materials can generate a localized piezoelectric field near the electrode surface under applied mechanical pressure.[33] Upon the application of compressive stress, a piezoelectric field directed from the cathode to the anode is established. This piezoelectric field can function as an "ion pump," facilitating ion migration and ensuring a more uniform ion distribution across the electrode surface.[34–36]

Considering that Zn^{2+} is a representative Lewis acid, the tetraethylammonium perchlorate (TEACC) additive was introduced into the aqueous electrolyte to regulate the solvation structure of Zn^{2+}. Based on the Lewis acid–base theory, TEACC partially replaces H_2O molecules in the solvation sheath, forming a solvation structure of $Zn(H_2O)_{4.8}(TEACC)_{0.2}(OTF)_1$. Moreover, TEACC molecules exhibit strong charge transfer interactions with the Zn anode, preferentially adsorbing onto its surface to generate a TEACC–OTF enriched electric double layer (EDL) and a robust solid electrolyte interphase (SEI). This dual-layer structure effectively modulates the Zn^{2+} distribution gradient and nucleation behavior on the anode surface, achieving an exceptional cycling stability of up to 3500 h, and this performance surpasses that of previously reported studies based on similar principles (Table S1, ESI†). The assembled $Zn\|TBABr_3$ battery demonstrates a remarkable capacity retention rate of 92.94%. Additionally, two large-format soft-pack batteries connected in series successfully powered 32 LED bulbs, highlighting their substantial potential for practical applications in flexible electronic devices. Finally, we believe that this work offers a new perspective on the significant application potential of ferroelectric molecules in AZIBs.

2. Results and discussion

2.1 Intrinsic properties of the electrolyte

The chemical structure of tetraethylammonium perchlorate (TEACC), a ferroelectric small molecule, is shown in Fig. S1 (ESI†). The electrostatic potential (ESP) of TEACC is depicted in Fig. 1a, in which the TEACC molecule contains more negatively charged functional groups compared to H_2O, facilitating stronger interactions between TEACC and Zn^{2+}, thereby incorporating it into the solvation structure of Zn^{2+}. As shown in the energy level diagram (Fig. 1b), the energy gap between the highest occupied molecular orbital (HOMO) and the lowest unoccupied molecular orbital (LUMO) of the TEACC molecule is narrower, and its LUMO level is significantly lower (−4.5 eV *vs.* −7.24 eV). This indicates that the TEACC molecule can more readily accept electrons and be reduced to form a solid electrolyte interphase (SEI) prior to the reduction of H_2O molecules. In the Fourier transform infrared spectrum (FT-IR, Fig. 1c), as the content of TEACC increases, the characteristic vibration peak of H–O stretching in H_2O (3200–3400 cm^{-1}) shifts slightly to a higher wavenumber. This indicates the formation of a hydrogen bonding network between H_2O and the oxygen atoms in TEACC, which have higher electronegativity. The stronger electron-withdrawing effect and the formation of new O(TEACC)–H(H_2O) covalent bonds, which are stronger than the original hydrogen bonds between H_2O, result from the higher negative charge density of the oxygen atoms in TEACC compared to those in H_2O. The absorption peak at 1100 cm^{-1} in the infrared spectrum corresponds to the –C–O– bond stretching vibration, indicating that TEACC retains their molecular form in the electrolyte without dissociating into ions. Fig. 1d presents the ^1H nuclear magnetic resonance (NMR) spectra of the electrolyte with different concentrations of the TEACC. As the additive content increases, the proton peaks shift downfield to higher chemical shifts. This shift is attributed to the disruption of the original hydrogen bonding network by the additive, leading to a reduction in the electron cloud density around the hydrogen atoms. Consequently, the

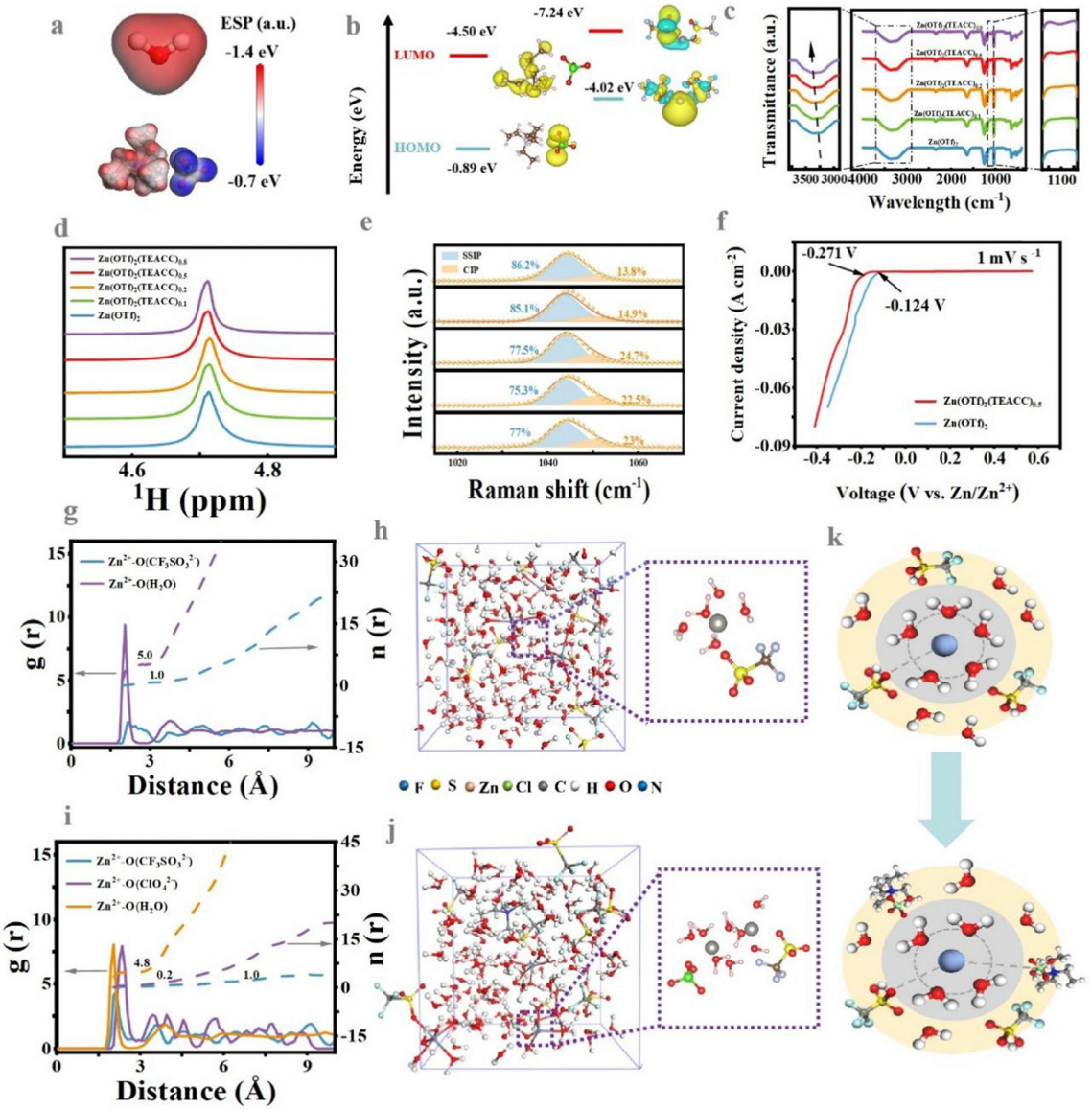

Fig. 1 (a) Electrostatic potential (ESP) map of H_2O and TEACC. (b) HOMO and LUMO energy levels of $Zn(OTf)_2$ and TEACC. (c) The FT-IR spectra, (d) the ^1H (H_2O) chemical shifts and (e) Raman spectra of $Zn(OTf)_2$, $Zn(OTf)_2(TEACC)_{0.1}$, $Zn(OTf)_2(TEACC)_{0.2}$, $Zn(OTf)_2(TEACC)_{0.5}$ and $Zn(OTf)_2(TEACC)_{0.8}$ electrolytes. (f) Electrochemical stability window of $Zn(OTf)_2$ and $Zn(OTf)_2(TEACC)_{0.5}$ electrolytes. Radial distribution function (RDF) $g(r)$ (solid curves) and corresponding coordination number $n(r)$ (dashed curves) for Zn^{2+}–$H_2O(O)$, Zn^{2+}–TEACC(O), and Zn^{2+}–$OTf^-(O)$ in (g) $Zn(OTf)_2$ and (i) $Zn(OTf)_2(TEACC)_{0.5}$ electrolytes obtained by MD simulations, snapshots during MD simulations and the corresponding Zn^{2+} solvation sheath in (h) $Zn(OTf)_2$ and (j) $Zn(OTf)_2(TEACC)_{0.5}$ electrolytes. (k) Diagram of the Zn^{2+} solvation structure.

proton transport rate in the electrolyte is lowered, which helps mitigate side reactions induced by H_2O molecules. Raman spectroscopy was employed to analyze the structural evolution of electrolytes with different compositions (Fig. 1e). The Raman characteristic peaks in the fingerprint region (1000–1100 cm^{-1}) were deconvoluted, with two distinct peaks representing solvent-separated ion pairs (SSIP, Zn^{2+}–OTF^-–xTEACC–$y$$H_2O$) and contact ion pairs (CIP, Zn^{2+}–OTF^-). As the additive content increased, the proportion of SSIP decreased, while the proportion of CIP increased. This shift caused the LUMO to transition from the solvent to the anion, resulting in the preferential decomposition of the anion and the formation of an inorganic-rich SEI, which can promote more uniform zinc deposition and this will be discussed in detail in Section 2.4. Benefiting from the excellent properties of the electrolyte, the hydrogen evolution potential of the $Zn(OTf)_2(TEACC)_{0.5}$ electrolyte extended from −0.124 V to −0.271 V, resulting in a reduced activity of free H_2O. This phenomenon is further demonstrated by the galvanostatic charge–discharge performance of the Zn‖Zn symmetric battery. In the $Zn(OTf)_2$ electrolyte, the anode becomes visibly blackened, with numerous pits and bubbles forming on its surface. In contrast, the anode maintains a smoother, denser surface in the $Zn(OTf)_2(TEACC)_{0.5}$ electrolyte (Fig. S2, ESI†).

The evolution of the solvation structure of the electrolyte with the addition of the additive was further quantified and analyzed using statistical molecular dynamics (MD) simulations. Radial distribution functions (RDFs) and coordination numbers (CNs) were employed for theoretical calculations of the $Zn(OTf)_2(TEACC)_{0.5}$ and $Zn(OTf)_2$ electrolytes. Fig. 1g illustrates the specific coordination environment in the $Zn(OTf)_2$ electrolyte. The first solvation shell of Zn^{2+} shows a peak at 1.92 Å, corresponding to a Zn–OH_2 coordination number of 5, and a peak at 1.95 Å, representing a Zn–OTf^- coordination number of 1. This confirms the formation of a $Zn(H_2O)_5^{2+}(OTf)^-$ solvation structure, as shown in Fig. 1h. In the $Zn(OTf)_2(TEACC)_{0.5}$ electrolyte, the Zn–OH_2 peak position remains unchanged, but the coordination number decreases to 4.8. The Zn–OTf^- coordination number remains at 1, with a slight peak shift to 1.92 Å. Additionally, a new peak at 1.92 Å appears, representing Zn–ClO_4 coordination with a coordination number of 0.2. These results indicate that TEACC molecules successfully replace some of H_2O in the first solvation shell of Zn^{2+}, forming a new solvation structure, $Zn(H_2O)_{4.8}(TEACC)_{0.2}(OTf)_2$, as shown in Fig. 1g. The schematic diagram of the specific solvation structure is shown in Fig. 1k.

The Zn^{2+} transference number reflects the ion transport capability. As shown in Fig. S3 (ESI†), it increases and then decreases with the addition of TEACC, but remains higher than that in the $Zn(OTf)_2$ electrolyte. The $Zn(OTf)_2(TEACC)_{0.5}$ electrolyte achieves the highest transference number of 0.79, indicating faster Zn^{2+} migration and reduced interference from other ions like H^+. The ion transport in the electrolyte is also related to the spatial volume occupied by the solvation structure. Smaller solvation structures are more favorable for Zn^{2+} transport. When the additive concentration reaches 0.8 M, more TEACC molecules may participate in the solvation structure, increasing the spatial volume of hydrated zinc ions, thereby affecting the Zn^{2+} transport process.

2.2 Double layer capacitance (EDL)

The electric double layer (EDL) structure, a critical feature at the electrode–electrolyte interface in zinc-ion batteries, comprises a compact layer and a diffuse layer, with the inner Helmholtz layer playing a pivotal role in determining battery performance, including cycling stability, power density, energy density, and charge–discharge efficiency. This study focuses on the influence of additives on the inner Helmholtz layer. As illustrated in Fig. 2a, the ferroelectric properties of TEACC molecules were characterized *via* piezo-response force microscopy (PFM) under voltages ranging from −4 V to 4 V. In high-voltage regions (<-1 V and >1 V), TEACC molecules exhibit stable amplitude and phase responses, attributed to the alignment of their polarization direction with the external electric field, thereby stabilizing the system. Conversely, near-zero voltages (−1 V to 1 V), both an amplitude and a phase display nonlinear behavior, marked by a sharp amplitude decrease and a 180° phase shift, indicative of the polarization reversal characteristic switching behavior of ferroelectric materials. These results demonstrate the effective electric field responsiveness of TEACC molecules, establishing a foundation for their use as additives in modulating the internal electric field of batteries. Furthermore, we assembled the TEACC material into an electrode and applied a constant force of approximately 10 N to investigate its voltage–current output characteristics. As shown in Fig. 2a–c, under this applied force, the TEACC electrode generated an average output current of 1 μA and a voltage of 13 V, demonstrating its ability to effectively convert mechanical pressure into electrical energy. Notably, while the pressure generated during the zinc deposition and stripping

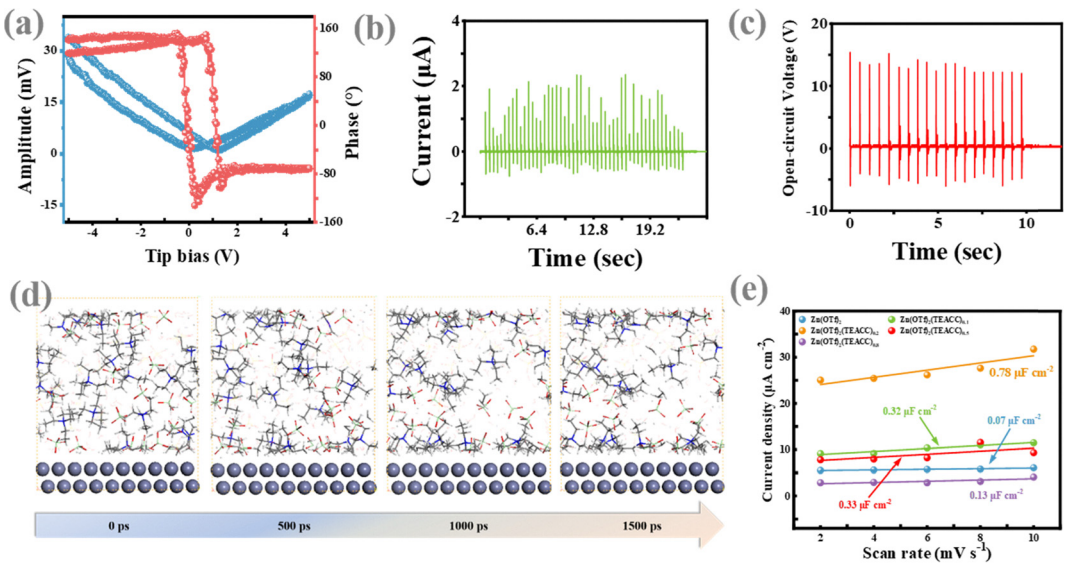

Fig. 2 (a) The butterfly curve and hysteresis loop of TEACC. (b) The output current and (c) output voltage of the TEACC electrode under the 10 N applied force. (d) The dynamic evolution of molecular adsorption in the $Zn(OTf)_2(TEACC)_{0.5}$ electrolyte. (e) The electric double layer capacitance diagram of the $Zn(OTf)_2(TEACC)_x$ electrolyte.

processes is inherently small, the resulting stress becomes significant due to the micron-scale thickness of the deposition/stripping layers. This phenomenon underscores the potential of TEACC as a functional material capable of harnessing the mechanical energy generated during battery operation. TEACC molecules, characterized by their high dielectric constant and abundant negatively charged functional groups, readily adsorb onto the Zn anode surface, thereby modifying the composition of the IHP. Given the experimental challenges in directly observing the Helmholtz layer, we employed molecular dynamics (MD) simulations in Materials Studio to model the adsorption dynamics at the electrolyte–anode interface (Fig. 2d). The simulations reveal that TEACC molecules gradually migrate toward the Zn anode, adsorb onto its surface, and progressively displace active H_2O within the IHP, ultimately forming a water-deficient interfacial structure. To further validate these findings, we performed CV tests to evaluate the electric double layer (EDL) capacitance of the $Zn(OTf)_2(TEACC)_x$ electrolytes. The introduction of TEACC enhances the EDL capacitance due to its high dielectric constant and larger atomic size, which facilitates its incorporation into the IHP. As illustrated in Fig. 2e, the $Zn(OTf)_2(TEACC)_x$ system exhibits a higher EDL capacitance compared to $Zn(OTf)_2$, providing indirect evidence that TEACC molecules effectively replace H_2O in the IHP; similarly, as shown in Fig. S4 (ESI†), the differential capacitance (DC) measurements further support the abovementioned conclusion. A schematic comparison of the Helmholtz layer structure in the $Zn(OTf)_2$ and $Zn(OTf)_2(TEACC)_{0.5}$ electrolytes is further depicted in Fig. S5 (ESI†).

The presence of H_2O in the Helmholtz layer is widely recognized as a primary cause of zinc metal corrosion, representing a critical failure mechanism in zinc batteries. To assess the corrosion inhibition capability of TEACC molecules, Tafel was performed on $Zn(OTf)_2(TEACC)_x$ electrolytes (Fig. S6 and Table S1, ESI†). Compared to the $Zn(OTf)_2$ electrolyte, the $Zn(OTf)_2(TEACC)_{0.5}$ system exhibits significantly enhanced anti-corrosion performance, as evidenced by a notably lower corrosion current density (-0.004 mA cm^{-2} *vs.* 0.152 mA cm^{-2}). Further insights into the effect of TEACC molecules on zinc deposition behavior were obtained through CA tests (Fig. S7, ESI†). Under an applied overpotential of -150 mV, the current density in the $Zn(OTf)_2$ electrolyte displayed a continuous increase, indicative of a predominant two-dimensional (2D) diffusion pathway for Zn^{2+} deposition. This growth mode is often associated with inhomogeneous deposition, promoting the formation of zinc dendrites. In contrast, the current density in the $Zn(OTf)_2(TEACC)_{0.5}$ electrolyte gradually stabilized, suggesting a successful transition from 2D to a more uniform three-dimensional (3D) diffusion mode following the initial nucleation of small zinc particles. This shift in the deposition mechanism is critical for achieving homogeneous zinc deposition and effectively suppressing dendrite formation.

2.3 Reversibility of zinc deposition and stripping

Galvanostatic cycling (GCD) tests were performed on Zn‖Zn symmetric batteries using $Zn(OTf)_2(TEACC)_x$ electrolytes with a current density of 1 mA cm^{-2} and an areal capacity of 0.5 mAh cm^{-2}. The Zn‖Zn symmetric cell with the $Zn(OTf)_2$ electrolyte exhibited the highest electrode polarization with an overpotential of approximately 0.1 V and experienced short-circuit failure after 200 h of cycling. In contrast, the Zn‖Zn symmetric battery with the $Zn(OTf)_2(TEACC)_{0.5}$ electrolyte demonstrated significantly lower polarization with an overpotential of around 0.05 V and achieved the longest cycling life, exceeding 3500 h (Fig. 3a). Even at higher current densities, the Zn‖Zn symmetric cell with the $Zn(OTf)_2(TEACC)_{0.5}$ electrolyte exhibited superior cycling performance (Fig. S8, ESI†). Consequently, the $Zn(OTf)_2(TEACC)_{0.5}$ electrolyte was identified as the optimal sample for further investigation of its underlying optimization mechanism. Long-term cycling tests demonstrated that TEACC molecules played a crucial role in regulating the solvation structure and reducing polarization. Cyclic voltammetry tests (CV, Fig. S9, ESI†) showed that all electrolytes exhibited stable reversibility after the initial two cycles. The $Zn(OTf)_2(TEACC)_{0.5}$ electrolyte displayed the smallest redox peak area, while larger peak areas in other electrolytes indicated a greater number of electrons transferred during the redox process. This increase in the peak area was attributed to side reactions, leading to overlapping currents with the original redox peaks, which was further confirmed by XRD analysis (Fig. 3c). Furthermore, the reversibility of zinc deposition and stripping was further evaluated using the Zn‖Cu battery under a current density of 1 mA cm^{-2}, an areal capacity of 0.5 mAh cm^{-2}, and a cutoff voltage of 0.5 V, as shown in Fig. 3b. The Zn‖Cu battery with the $Zn(OTf)_2(TEACC)_{0.5}$ electrolyte exhibited an initial nucleation overpotential of 70 mV, which increased to 120 mV after the cycling stabilized. Higher nucleation overpotential suggests an enhanced nucleation driving force, facilitating finer zinc deposition. In contrast, a lower nucleation overpotential may accelerate dendritic growth due to the "tip effect." The surface and cross-sectional morphologies of the Zn electrode after 100 cycles under a current density of 1 mA cm^{-2}, and an areal capacity of 0.5 mAh cm^{-2} were further examined using scanning electron microscopy (SEM, Fig. 3d). The zinc electrode deposited from the $Zn(OTf)_2$ electrolyte exhibited a porous morphology with an uneven surface featuring numerous small protrusions, which were identified as zinc dendrites under higher magnification (Fig. S10, ESI†). In contrast, the electrode deposited from the $Zn(OTf)_2(TEACC)_{0.5}$ electrolyte displayed a remarkably smooth and uniform surface without any visible by-products or dendrites. Notably, the TEACC-modified electrolyte produced a dense and compact deposition layer with a thickness of 66.2 μm, significantly thinner than the 96.4 μm layer formed in the conventional electrolyte.

XRD characterization (Fig. 3c) provides critical insights into the composition and crystallographic orientation of deposited zinc electrodes. In the $Zn(OTf)_2(TEACC)_{0.5}$ electrolyte, a ZnS peak appeared around 30°, indicating the formation of ZnS, which serves as a foundation for constructing a robust solid electrolyte interphase (SEI). Additionally, the (002) crystal plane of Zn exhibited the strongest peak in the $Zn(OTf)_2(TEACC)_{0.5}$

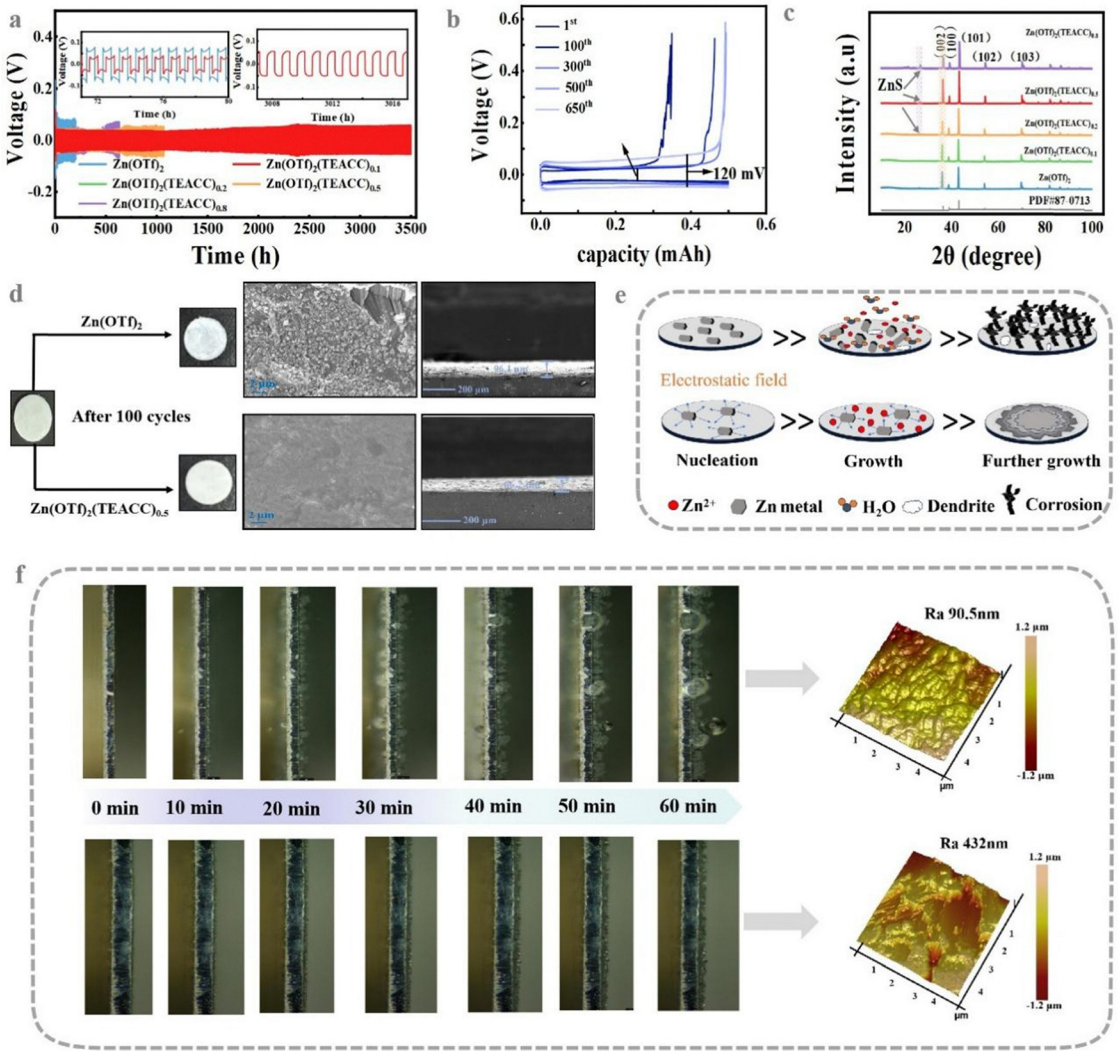

Fig. 3 (a) Zn plating/stripping in Zn‖Zn symmetrical cells using the $Zn(OTf)_2(TEACC)_x$ electrolyte at current density of 1 mA cm^{-2} with an areal capacity of 0.5 mAh cm^{-2}. (b) Voltage curves of the Zn‖Cu asymmetric cells for selected cycles in the $Zn(OTf)_2(TEACC)_{0.5}$ electrolyte. (c) XRD spectra of zinc deposited on the anode after cycling. (d) Top-view SEM images and cross-sectional SEM images of the Zn electrode after 100 cycles with $Zn(OTf)_2$ and $Zn(OTf)_2(TEACC)_{0.5}$ electrolytes. (e) Schematic diagram of the growth mechanism. (f) *In situ* optical microscopy and AFM images of the cross-sectional Zn deposition morphology on the Zn foil with plating times in $Zn(OTf)_2(TEACC)_x$ electrolytes at 5 mA cm^{-2}.

sample. The preferential growth along the (002) plane facilitates zinc deposition parallel to the substrate, contributing to the formation of a uniform and dense deposition layer. *In situ* optical microscopy and AFM (Fig. 3f) reveal striking contrasts between electrolyte systems. Under 5 mA cm^{-2} deposition current, the $Zn(OTf)_2$ electrolyte exhibits progressive dendrite formation after 20 minutes, accompanied by persistent hydrogen evolution evidenced by growing gas bubbles. Conversely, the $Zn(OTf)_2(TEACC)_{0.5}$ system maintains exceptional morphological stability, showing only thickness-increase deposition without any dendritic features.

2.4 Solid electrolyte interphase (SEI) composition

To gain further insight into the structure and composition of the SEI formed in the $Zn(OTf)_2(TEACC)_{0.5}$ electrolyte, transmission electron microscopy (TEM) and X-ray photoelectron spectroscopy (XPS) analyses were performed. The TEM images (Fig. 4a–g) clearly reveal the formation of a distinct SEI layer on the Zn anode (the thickness of the SEI layer is approximately 22–30 nm, Fig. S11, ESI†), with a smooth edge morphology attributed to volume shrinkage caused by electron beam damage. This characteristic suggests the presence of organic components within the SEI. Additionally, lattice fringes corresponding to ZnO(100), ZnS(111), and $ZnCO_3$(006) were identified, indicating the formation of multiple inorganic phases. XPS combined with Ar^+ sputtering was further employed to investigate the depth-resolved composition of the SEI layer after 50 cycles.

Fig. 4h presents the XPS spectra of the C 1s, O 1s, N 1s, S 2p, and Cl 2p regions at sputtering times of 5 min, 10 min, 15 min, and 20 min. The C 1s spectrum predominantly exhibited three distinct components, corresponding to $ZnCO_3$ (289.38 eV), C–

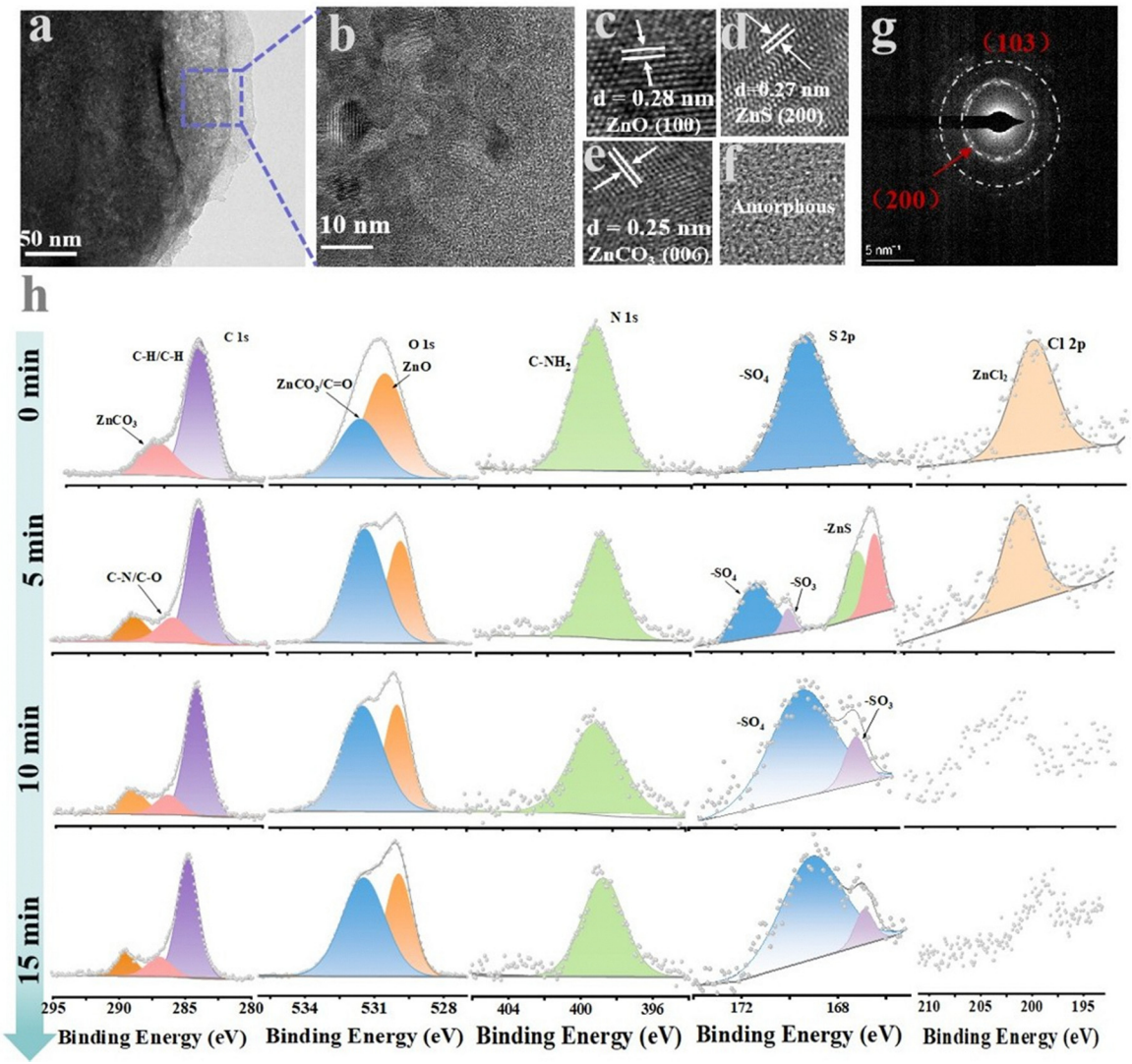

Fig. 4 (a) and (b) TEM, (c)–(f) HR-TEM images and (g) SAED of the SEI formed in $Zn(OTf)_2(TEACC)_{0.15}$ electrolytes after 50 cycles. (h) High resolution XPS spectra of C 1s, O 1s, N 1s, S 2p and Cl 2p after Ar^+ sputtering for 0, 5, 10 and 15 min.

N/C–O (286.6 eV), and C–C/C–H (284.8 eV). The O 1s spectrum displayed two characteristic peaks attributed to ZnO (529.78 eV) and $ZnCO_3$ (531.56 eV), further confirming the presence of $ZnCO_3$. The N 1s and Cl 2p spectra each exhibited a single peak, assigned to $C–NH_2$ (398.96 eV) and $ZnCl_2$ (199.47 eV), respectively. These species are attributed to the decomposition of the TEACC additive. The S 2p spectrum presented a more complex profile. At the surface, only a sulfate ($–SO_4$) peak was detected. However, after 5 minutes of sputtering, the S 2p spectrum showed the presence of three components: $–SO_4$ (169.11 eV), $–SO_3$(166.20 eV), and ZnS (162.00 eV). Notably, the ZnS signal gradually diminished with increasing sputtering time. $ZnCO_3$, ZnO, and $ZnCl_2$ were identified as representative inorganic components, while C–H, C–C, and $C–NH_2$ were indicative of the organic fraction. The inorganic components were found to be more abundant than the organic ones, facilitating efficient Zn^{2+} transport and uniform deposition. This dual-phase organic/inorganic SEI layer originates from the electrochemical reduction and decomposition of TEACC and OTf^-. Importantly, it enables Zn^{2+} migration while effectively isolating the Zn anode surface from water molecules, thereby mitigating side reactions and suppressing dendrite growth.

2.5 $Zn\|TBABr_3$ full batteries

Fig. 5a shows the CV curves of the $Zn\|TBABr_3$ full cell using $Zn(OTf)_2(TEACC)_{0.5}$ as the electrolyte at different scan rates, within a voltage range of 0.8 V to 2.1 V. All the CV curves exhibit a distinct reduction peak ($Br^0 \rightarrow Br^-$, 1.64 V) and an oxidation peak ($Br^- \rightarrow Br^0$, 1.8 V). The well-defined redox peaks remain evident even at high scan rates, indicating that the $Zn\|TBABr_3$ cell with the $Zn(OTf)_2(TEACC)_{0.5}$ electrolyte exhibits fast ion/electron transport kinetics and excellent structural stability. The *b*-values approaching 1 suggests that the redox process is primarily dominated by capacitive behavior (Fig. 5b). This further implies a rapid ion diffusion rate in the electrolyte, effectively minimizing diffusion limitations and enhancing

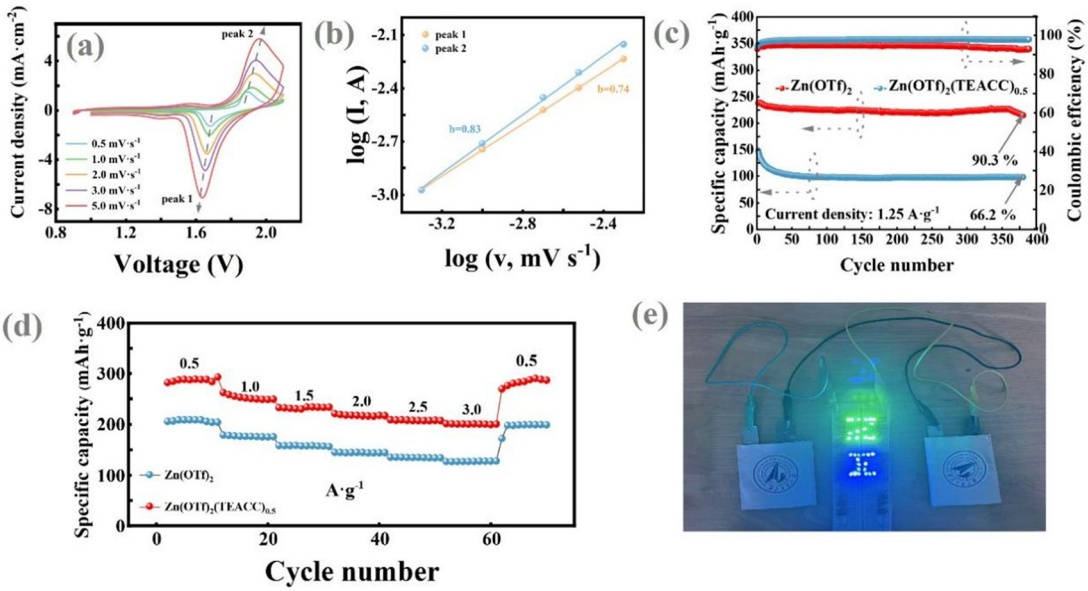

Fig. 5 (a) CV curves of the Zn‖TBABr$_3$ cell using the Zn(OTf)$_2$(TEACC)$_{0.5}$ electrolyte at different scan rates. (b) The *b* values of different peaks. (c) Long-term cycling of the Zn‖TBABr$_3$ full cells at Zn(OTF)$_2$ and Zn(OTF)$_2$(EDTACC)$_{0.5}$ electrolytes at current density of 1.25 A g^{-1}. (d) Rate performance of Zn‖TBABr$_3$ batteries using Zn(OTF)$_2$ and Zn(OTF)$_2$(EDTACC)$_{0.5}$ electrolytes. (e) Digital photograph of the lighted 23 LED lights powered by 2 Zn‖TBABr$_3$ batteries.

reaction kinetics. Fig. S11 (ESI†) illustrates the discharge capacities of Zn‖TBABr$_3$ full cells using different electrolytes at a current density of 1 A g^{-1}. The initial discharge specific capacities are 143.1 mAh g^{-1}, 226.5 mAh g^{-1}, 132.3 mAh g^{-1}, 265.1 mAh g^{-1} and 226.5 mAh g^{-1}. These results demonstrate that the unique solvation structure and the formation of an inner Helmholtz plane (IHP) facilitated by TEACC significantly enhance the reaction kinetics of the TBABr$_3$, leading to improved discharge capacity.

Fig. 5c presents the long-term cycling performance of Zn‖TBABr$_3$ full cells with Zn(OTf)$_2$ and Zn(OTf)$_2$(TEACC)$_{0.5}$ electrolytes under a constant current density of 1.25 A g^{-1}. When using the Zn(OTf)$_2$(TEACC)$_{0.5}$ electrolyte, the initial discharge specific capacity reaches 238.2 mAh g^{-1} with a first-cycle coulombic efficiency of 92.94%. Even after 380 cycles, the discharge specific capacity remains at 215.1 mAh g^{-1}, corresponding to a capacity retention of 90.3%. In contrast, the Zn(OTf)$_2$ electrolyte results in a much lower initial discharge specific capacity of 148.2 mAh g^{-1}, which declines to 97.8 mAh g^{-1} after 100 cycles, with a capacity retention of only 66.2%. The significant improvement in capacity retention can be attributed to the high dielectric constant and intrinsic ferroelectric properties of TEACC. These properties effectively promote the decoupling of zinc triflate salts in the electrolyte, enhancing Zn^{2+} mobility and accelerating the reaction kinetics. To evaluate the discharge performance of Zn‖TBABr$_3$ batteries under various current densities, rate capability tests were conducted. As shown in Fig. 5d, the current density was progressively increased from 0.5 A g^{-1} to 3 A g^{-1} and then decreased back to 0.5 A g^{-1}. The corresponding voltage profiles at each current density are presented in Fig. S12 (ESI†). Using the Zn(OTf)$_2$(TEACC)$_{0.5}$ electrolyte, the reversible charge–discharge capacities at current densities of 0.5, 1, 1.5, 2, 2.5, and 3 A g^{-1} were 282.1, 258.4, 232.1, 220.9, 208.3 and 220.8 mAh g^{-1}, respectively, exhibiting significantly superior performance compared to Zn‖TBABr$_3$ batteries with the Zn(OTf)$_2$ electrolyte. This enhancement can be attributed to the unique solvation structure of TEACC, which effectively suppresses Zn dendrite growth and mitigates the HER. Consequently, side reactions at the bromine electrode are reduced, allowing the Zn‖TBABr$_3$ battery to maintain high discharge capacities across a range of current densities. To further assess the practical applicability of the TEACC-containing electrolyte in flexible devices and large-scale energy storage, a Zn‖TBABr$_3$ pouch cell was assembled. The open-circuit voltage (OCV) of a single pouch cell was approximately 1.7 V. To achieve a higher operating voltage, two identical pouch cells were connected in series, successfully powering 32 LED bulbs (Fig. 5e and Fig. S13, ESI†). This demonstration underscores the promising potential of Zn‖TBABr$_3$ batteries for large-scale energy storage applications.

3 Conclusions

By incorporating TEACC ferroelectric molecules, H_2O molecules in the Zn^{2+} solvation structure are partially displaced, resulting in the formation of a TEACC–OTf^- rich electrode/electrolyte interface. Additionally, TEACC molecules substitute H_2O in the IHP, creating a water-deficient inner Helmholtz plane (IHP). This unique solvation structure reduced the activity of free H_2O molecules, enhanced the Zn^{2+} transport rate in the electrolyte, and promoted the formation of the SEI rich in inorganic components such as $ZnCO_3$, $ZnCl_2$, and ZnS.

Consequently, highly reversible Zn deposition and stripping without dendrite growth were achieved. The water-deficient IHP further minimized the direct contact between H_2O molecules and the zinc anode, effectively suppressing the HER and extending the hydrogen evolution potential from −0.124 V to −0.271 V. Moreover, the distinctive ferroelectric properties of TEACC facilitated the decoupling of zinc triflate salts in the electrolyte. Combined with the stress induced by the Zn deposition and stripping processes, this promoted the formation of a uniform Zn^{2+} concentration gradient. As a result, the Zn‖$TBABr_3$ battery demonstrated an outstanding capacity retention of 92.94%. Additionally, two large pouch cells connected in series successfully powered 32 LED bulbs, highlighting the significant potential of Zn‖$TBABr_3$ batteries for practical applications in flexible and large-scale energy storage systems.

Author contributions

Lixin Song: data curation, visualization, investigation, and writing – original draft. Ruizhe Zhang: writing – review, editing and investigation. Zhiyong Liao: conceptualization, methodology, and software. Yongbo Fan: supervision. Yawen Li: conceptualization and supervision. Longtao Ma: conceptualization, methodology, and writing – review and editing. Huiqing Fan: project administration, supervision, and funding acquisition.

Conflicts of interest

There are no conflicts to declare.

Data availability

The data sets used and/or analyzed during the current study are available from the corresponding author upon reasonable request.

Acknowledgements

This work was supported by the National Nature Science Foundation (52372125 and 52333009), the Shaanxi Provincial Science Foundation (2021GXLH-01-11), the Yulin Project (2022-19-11), the High-Quality Patent Cultivation Project (XGD2021-04), the Fundamental Research Funds for the Central Universities (D5000230071), and the 111 Program of MOE of China (B08040). We would also like to thank the National Natural Science Foundation of China (52202299) and the Analytical & Testing Center of Northwestern Polytechnical University (2024T008).

References

1 J. K. Kirkegaard, D. P. Rudolph and S. Nyborg, *et al.*, Tackling grand challenges in wind energy through a socio-technical perspective, *Nat. Energy*, 2023, **8**(7), 655–664.
2 L. Ma, S. Chen and W. Yan, *et al.*, A high-energy aqueous Zn‖NO_2 electrochemical cell: a new strategy for NO_2 fixation and electric power generation, *Energy Environ. Sci.*, 2023, **16**, 1125–1134.
3 L. Kruitwagen, K. T. Story and J. Friedrich, *et al.*, A global inventory of photovoltaic solar energy generating units, *Nature*, 2021, **598**(7882), 604–610.
4 X. Wang, X. Li and H. Fan, *et al.*, Solid electrolyte interface in Zn-based battery systems, *Nano-Micro Lett.*, 2022, **14**, 205.
5 M. Chuai, J. Yang and M. Wang, *et al.*, High-performance Zn battery with transition metal ions co-regulated electrolytic MnO2, *eScience*, 2021, **1**(2), 178–185.
6 X. Wang, K. Feng and B. Sang, *et al.*, Highly reversible zinc metal anodes enabled by solvation Structure and interface chemistry modulation, *Adv. Energy Mater.*, 2023, **13**, 2301670.
7 X. Li, X. Wang and L. Ma, *et al.*, Solvation structures in aqueous metal-ion batteries, *Adv. Energy Mater.*, 2022, **12**(37), 2202068.
8 Y. Wang, Z. Wang and W. K. Pang, *et al.*, Solvent control of water O-H bonds for highly reversible zinc ion batteries, *Nat. Commun.*, 2023, **14**(1), 2720.
9 L. Ma, S. Chen and N. Li, *et al.*, Hydrogen-free and dendrite-free all-solid-state Zn-ion batteries, *Adv. Mater.*, 2020, **32**(14), e1908121.
10 J. Shi, T. Sun and J. Bao, *et al.*, ''water-in-deep eutectic solvent'' electrolytes for high-performance aqueous Zn-ion batteries, *Adv. Funct. Mater.*, 2021, **31**(23), 2102035.
11 H. Bian, C. Wang and Y. Wang, *et al.*, Phase Inversion-Induced Porous Polymer Coating for High Rate and Stable zinc anode, *Adv. Funct. Mater.*, 2024, **240**, 2401760.
12 Y. Liang, H. Dong and D. Aurbach, *et al.*, Current status and future directions of multivalent metal-ion batteries, *Nat. Energy*, 2020, **5**(9), 646–656.
13 Y. Huang, Z. Chang and W. Liu, *et al.*, Layer-by-layer zinc metal anodes to achieve long-life zinc-ion batteries, *Chem. Eng. J.*, 2022, **431**(1), 01–09.
14 Q. Cao, Y. Gao and J. Pu, *et al.*, Gradient design of imprinted anode for stable Zn-ion batteries, *Nat. Commun.*, 2023, **14**(1), 641.
15 H. Dou, M. Xu and Y. Zheng, *et al.*, Bioinspired tough solid-state electrolyte for flexible ultralong-life Zinc-air battery, *Adv. Mater.*, 2022, **34**(18), e2110585.
16 J. Shi, S. Wang and X. Chen, *et al.*, An ultrahigh energy density quasi-solid-state Zinc ion microbattery with excellent flexibility and thermostability, *Adv. Energy Mater.*, 2019, **9**(37), e1901957.
17 Z. Liu, Q. Yang and D. Wang, *et al.*, A flexible solid-state aqueous Zinc hybrid battery with flat and high-voltage discharge plateau, *Adv. Energy Mater.*, 2019, **9**(46), e1902473.
18 L. Ma, S. Chen and N. Li, *et al.*, Hydrogen-free and dendrite-free all-solid-state Zn-ion batteries, *Adv. Mater.*, 2020, **32**(14), e1908121.
19 J. Wang, J. X. Tian and G. X. Liu, *et al.*, In situ insight into the interfacial dynamics in ''water-in-salt'' electrolyte-based aqueous zinc batteries, *Small Methods*, 2023, **7**(6), e2300392.
20 Z. Zhao, J. Lai and D. T. Ho, *et al.*, A novel ''water-in-ionic liquid'' electrolyte for Zn metal batteries, *ACS Energy Lett.*, 2022, **8**(1), 608–618.

21 L. Zhang, I. A. Rodríguez-Pérez and H. Jiang, *et al.*, $ZnCl_2$ ''water-in-salt'' electrolyte transforms the performance of vanadium oxide as a Zn battery cathode, *Adv. Funct. Mater.*, 2019, **29**(30), e1902653.
22 Y. Jiao, F. Li and X. Jin, *et al.*, Engineering polymer glue towards 90% Zinc utilization for 1000 hours to make high-performance Zn-ion batteries, *Adv. Funct. Mater.*, 2021, **31**(49), e2107652.
23 Y. Wu, T. Zhang and L. Chen, *et al.*, Polymer chain-guided ion transport in aqueous electrolytes of Zn-ion batteries, *Adv. Energy Mater.*, 2023, **13**(29), e2300719.
24 L. Yan, Q. Zhu and Y. Qi, *et al.*, Towards high-performance aqueous Zinc batteries via a semi-conductive bipolar-type polymer cathode, *Angew. Chem., Int. Ed.*, 2022, **61**(42), e202211107.
25 F. Bu, Y. Gao and W. Zhao, *et al.*, Bio-inspired trace hydroxyl-rich electrolyte additives for high-rate and stable Zn-ion batteries at low temperatures, *Angew. Chem., Int. Ed.*, 2024, **63**(9), e202318496.
26 R. Chen, W. Zhang and Q. Huang, *et al.*, Trace amounts of triple-functional additives enable reversible aqueous Zinc-ion batteries from a comprehensive perspective, *Nano-Micro Lett.*, 2023, **15**(1), 81.
27 R. Sun, D. Han and C. Cui, *et al.*, A self-deoxidizing electrolyte additive enables highly stable aqueous Zinc batteries, *Angew. Chem., Int. Ed.*, 2023, **62**(28), e202303557.
28 F. Ming, Y. Zhu and G. Huang, *et al.*, Co-solvent electrolyte engineering for stable anode-free zinc metal batteries, *J. Am. Chem. Soc.*, 2022, **144**(16), 7160–7170.
29 J. Shi, T. Sun and J. Bao, *et al.*, ''Water-in-deep eutectic solvent'' electrolytes for high-performance aqueous Zn-ion batteries, *Adv. Funct. Mater.*, 2021, **31**(23), 2102035.
30 S. Wang, G. Liu and W. Wan, *et al.*, Acetamide-caprolactam deep eutectic solvent-based electrolyte for stable Zn–metal batteries, *Adv. Mater.*, 2023, **36**(5), e2306546.
31 C. Chang, M. Zhang and Z. Lao, *et al.*, Achieving stable lithium anodes through leveraging inevitable stress variations via adaptive piezoelectric effect, *Adv. Mater.*, 2024, **36**(19), 2313525.
32 N. Li, K. Xie and H. Huang, Ferroelectric materials for high energy density batteries: progress and outlook, *ACS Energy Lett.*, 2023, **8**(10), 4357–4370.
33 A. Li, Y. Wang and H. Tian, *et al.*, Multifunctional properties of a polar spin chain compound $[N(C_3H_7)_4][Cu(C_8H_4NO_4)]\cdot H_2O$ exhibiting both one-dimensional magnetism and nonlinear optical activity, *Chin. Chem. Lett.*, 2024, **35**(2), 108780.
34 J. Tao, Y. Chen and A. Bhardwaj, *et al.*, Combating Li metal deposits in all-solid-state battery via the piezoelectric and ferroelectric effects, *Proc. Natl. Acad. Sci. U. S. A.*, 2022, **119**(41), e2211059119.
35 C. Wang, M. Liu and M. Thijs, *et al.*, High dielectric barium titanate porous scaffold for efficient Li metal cycling in anode-free cells, *Nat. Commun.*, 2021, **12**(1), 6536.
36 Q. Zong, B. Lv and C. Liu, *et al.*, Dendrite-free and highly stable Zn metal anode with $BaTiO_3$/P(VDF-TrFE) coating, *ACS Energy Lett.*, 2023, **8**(7), 2886–2896.

